Highly Proton-Conducting Lanthanide Metal-Organic Frameworks Featuring Highly Oxygenated ligands with Slow Magnetic Relaxation or Magnetocaloric Effect

Shun-Yi Yang, [a] Qian Zhang, [a] Yang-Lu Zhang, [a] Tie-Shen Tan, [a] Junlun Zhu, [a] Xiaodong Yang, [a] Le Shi, [b] Jiong Yang, [c,d] and Dong Shao *[a]

[a] *Hubei Key Laboratory of Processing and Application of Catalytic Materials, College of Chemistry and Chemical Engineering, Huanggang Normal University, Huanggang 438000, P. R. China*

[b] *State Key Laboratory of Chemical Engineering, Stoddart Institute of Molecular Science, Department of Chemistry, Zhejiang University, Hangzhou 310027, P. R. China*

[c] *Department of Chemistry, Southern University of Science and Technology (SUSTech), Shenzhen 518055, China*

[d] *Institut des Matériaux Poreux de Paris, Paris, PSL University, Paris, France*

Correspondence and requests for materials should be addressed to

Email: shaodong@nju.edu.cn

Table of Contents

EXPERIMENTAL SECTION 4

Figure S1. The photograph of a single crystal of the **Tb-MOF**. 7

Figure S2. The FT-IR spectrum of the **Tb-MOF**. 7

Figure S3. The photograph of a single crystal of **Gd-MOF**. 8

Figure S4. The FT-IR spectrum of the **Gd-MOF** 8

Figure S5 Asymmetry unit of **Tb-MOF**. 9

Figure S6 Asymmetry unit of **Gd-MOF** 9

Table S1. Continuous shape measure analysis for eight-coordinated Ln^{3+} in Tb-MOF and Gd-MOF. 10

Table S2. Selected bond lengths (Å) and angles [°] in Tb-MOF. 11

Table S3. Selected bond lengths (Å) and angles [°] in Gd-MOF. 12

Figure S7. Portion of the 3D framework structure of **Gd-MOF**. 13

Topological analysis 14

Figure S8. Comparison of the experimental PXRD pattern of **Tb-MOF** with the calculated pattern from the crystal structure. 15

Figure S9. Comparison of the experimental PXRD pattern of **Gd-MOF** with the calculated pattern from the crystal structure. 15

Figure S10. Termogravimetric analysis curve of **Tb-MOF** 16

Figure S11. Thermogravimetric analysis curve of **Gd-MOF** 16

Figure S12. N_2 adsorption isotherms of **Gd-MOF** measured at 77 K. 17

Figure S13. Water uptake of **Gd-MOF** measured at 300 K. 17

Figure S14. *M versus H* plot of **Tb-MOF** at 1.8 K. 18

Figure S15. *M versus H* plot of **Gd-MOF** at 1.8 K. 18

Figure S16. Frequency dependence of ac susceptibility measured under zero dc field at 2.0 K for **Gd-MOF**. 19

Figure S17. Frequency dependence of in-phase (χ′) signals ac susceptibility measured under zero dc field for **Tb-MOF**. 19

Figure S18. Frequency dependence of in-phase (χ′) signals ac susceptibility measured under different dc fields at 1.8 K for **Tb-MOF**. 20

Figure S19. Frequency dependence of in-phase (χ′) signals ac susceptibility measured under 2 kOe dc field for **Tb-MOF** 20

Table S4. Relaxation fitting parameters from the least-square fitting of the Cole-Cole plots of Tb-MOF under 2 kOe dc filed according to the generalized Debye model. 21

Figure S20. τ^{-1} vs T plot for **Tb-MOF**. The red line represents the fit via combined Orbach, Raman, and QTM relaxation mechanism. 21

Figure S21. M versus H plots of **Gd-MOF** measured at 2-10 K..... 22

Figure S22. Nyquist plots of **Gd-MOF** at 30 °C under different RHs. 23

Table S5. Proton conductivity of Tb-MOF and Gd-MOF at 30 °C under various RH. 23

Figure S23. The humidity dependent σ at 30 °C of **Tb-MOF**..... 24

Figure S24. The humidity dependent σ at 30 °C of **Gd-MOF**. 24

Figure S25. Nyquist plots of **Gd-MOF** measured under 98% RH at different temperature.. 24

Table S6. Proton conductivity of Tb-MOF and Gd-MOF at varying temperature under 98% RH. 25

Figure S26. ln(σ*T*) vs. 1000/*T* for **Gd-MOF** at 98% RH. 25

Figure S27. The FT-IR spectra of the **Tb-MOF** and **Gd-MOF** after electrochemical tests. 25

Figure S28. PXRD pattern of **Tb-MOF** after electrochemical tests. 26

Figure S29. PXRD pattern of **Gd-MOF** after electrochemical tests..... 26

Table S7. Some Reported Gd_2-based molecular coolants. 22

References 27

EXPERIMENTAL SECTION

Physical measurements

Infrared spectra were obtained in the range of 600–4000 cm^{-1} on a Bruker tensor II spectrometer. Elemental analyses of C, O, and H were performed at an Elementar Vario MICRO analyzer. Powder X-ray diffraction data (PXRD) were recorded on a Bruker D8 Advance diffractometer with Cu Kα X-ray source (λ = 1.54056 Å) operated at 40 kV and 40 mA between 5 and 35° (2θ). Thermal gravimetric analysis (TGA) was carried out on freshly filtered crystals using the Mettler Toledo TGA2 instrument in an insert Ar atmosphere over a temperature range of 27–700 °C with a heating rate of 10 °C/min. Low-pressure volumetric N_2 gas adsorption measurements were performed on a Quadrasorb automatic volumetric instrument. The Brunauer-Emmett-Teller (BET) method was utilized to calculate the specific surface areas. Water adsorption/desorption isotherms were measured using a BELSORP max instrument. Magnetic measurements were performed using a Quantum Design SQUID VSM magnetometer on the crushed samples from the single crystals of the compounds. Alternative current (ac) magnetic susceptibility data were collected in a zero dc field or an applied dc fields in the temperature range of 2-8 K, under an ac field of 2 Oe, oscillating at frequencies in the range of 1-1000 Hz. All magnetic data were corrected for the diamagnetic contributions of the sample holder and of core diamagnetism of the sample using Pascal's constants.

Proton conductivity

Proton conductivity measurements were performed using a quasi-four-electrode AC impedance technique with a Solartron 1260 impedance/gain-phase analyzer. The single

crystals samples were compressed to 2.2 mm diameter, which were connected to gold wires using silver paste. The sample pellet was measured in the temperature range of 30−55 °C and in the RH range of 50−98%. The samples were placed in Espec Corp. SH-221 incubator at a given temperature and relative humidity values for 2 hours before recording the impedance. The conductivity was calculated using the equation $\sigma = l/R_sA$, where l and A are the thickness (cm) and cross-sectional area (cm^2) of the pellet, respectively, and R_s is the bulk resistance of the sample. R_s was calculated using the Nyquist plot from impedance spectra.

X-ray Crystallography

Single crystal X-ray diffraction data were collected on a Bruker D8 QUEST diffractometer with a PHOTON III CMOS detector (Mo-K_α radiation, $\lambda = 0.71073$ Å). The APEX III program was used to determine the unit cell parameters and for data collection. The data were integrated and corrected for Lorentz and polarization effects using SAINT.[S1] Absorption corrections were applied with SADABS.[S2] The structures were solved by direct methods and refined by full-matrix least-squares method on $F2$ using the SHELXTL[S3] crystallographic software package integrated in Olex 2.[S4] All the non-hydrogen atoms were refined anisotropically. Hydrogen atoms of the organic ligands were refined as riding on the corresponding non-hydrogen atoms. Additional details of the data collections and structural refinement parameters are provided in Table 1. A solvent mask was calculated for Tb-MOF and 126 electrons were found in a volume of 442 A^3 per unit cell. This is consistent with the presence of 6[H_2O] per asymmetric unit which account for 120 electrons per unit cell. A solvent mask was

calculated for Gd-MOF and 68 electrons were found in a volume of 510 A^3 per unit cell. This is consistent with the presence of 6[H_2O] per asymmetric unit which account for 60 electrons per unit cell. Selected bond lengths and angles of **Tb-MOF** and **Gd-MOF** are listed in Table S1, S2. CCDC numbers 2326140 and 2326141 are the supplementary crystallographic data for this paper. They can be obtained freely from the Cambridge Crystallographic Data Centre via www.ccdc.cam.ac.uk/data_request/cif.

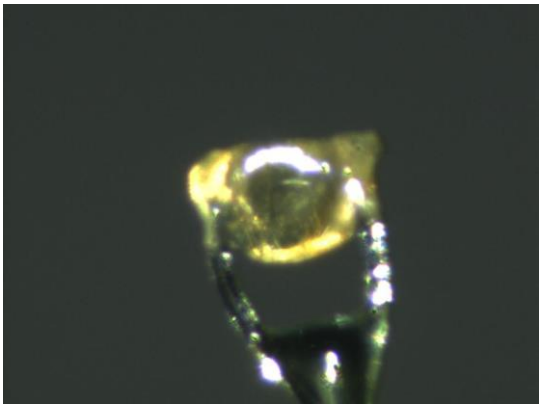

Figure S1. The photograph of a single crystal of the **Tb-MOF**.

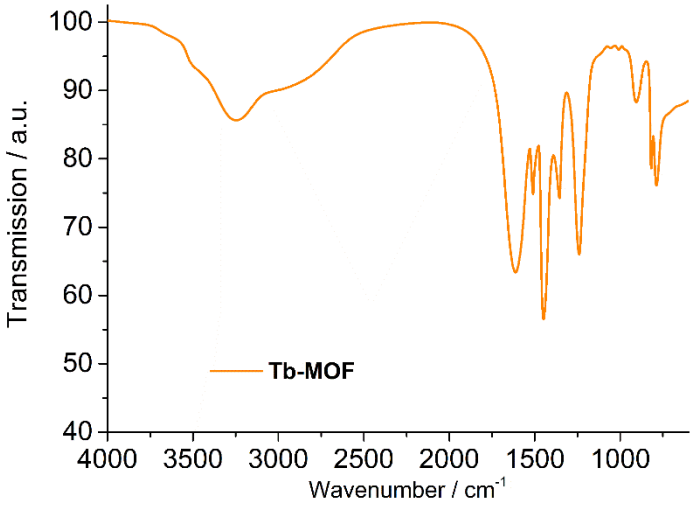

Figure S2. The FT-IR spectrum of the **Tb-MOF**.

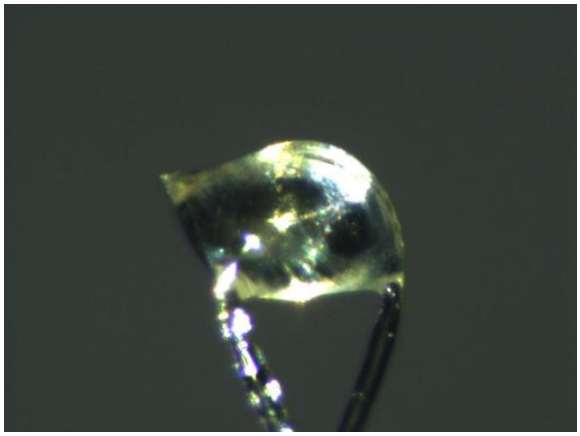

Figure S3. The photograph of a single crystal of **Gd-MOF**.

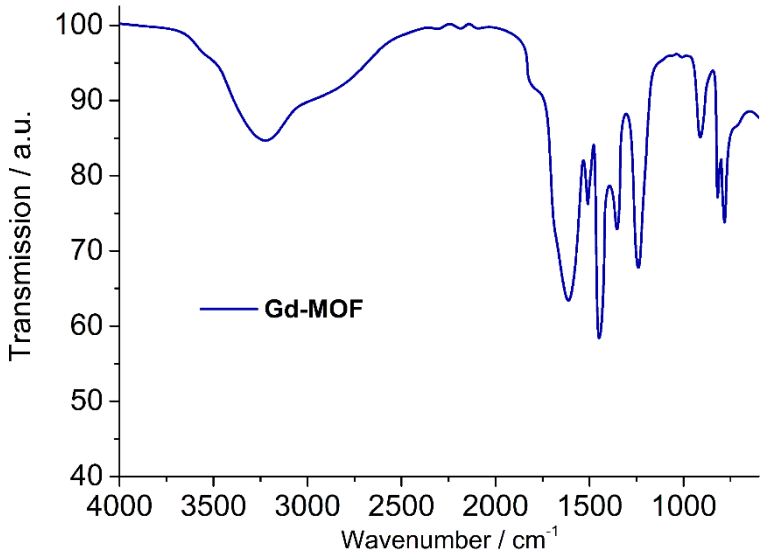

Figure S4. The FT-IR spectrum of the **Gd-MOF**.

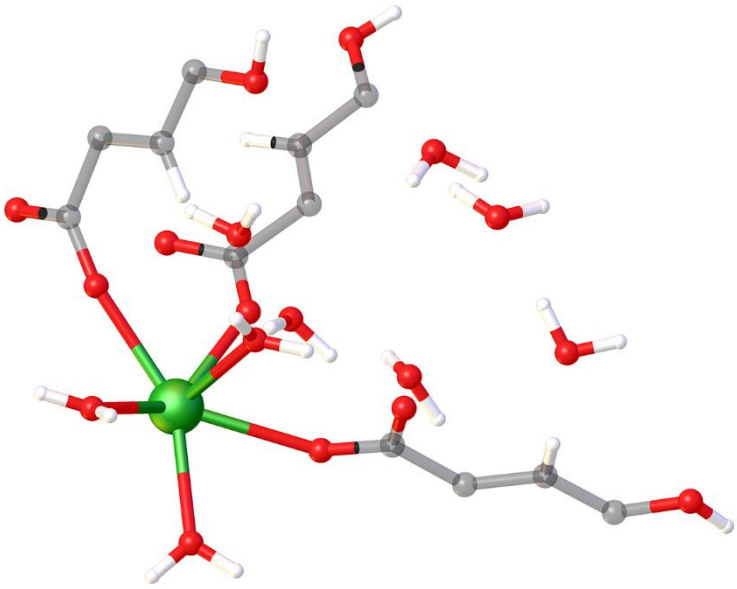

Figure S5 Asymmetry unit of **Tb-MOF**.

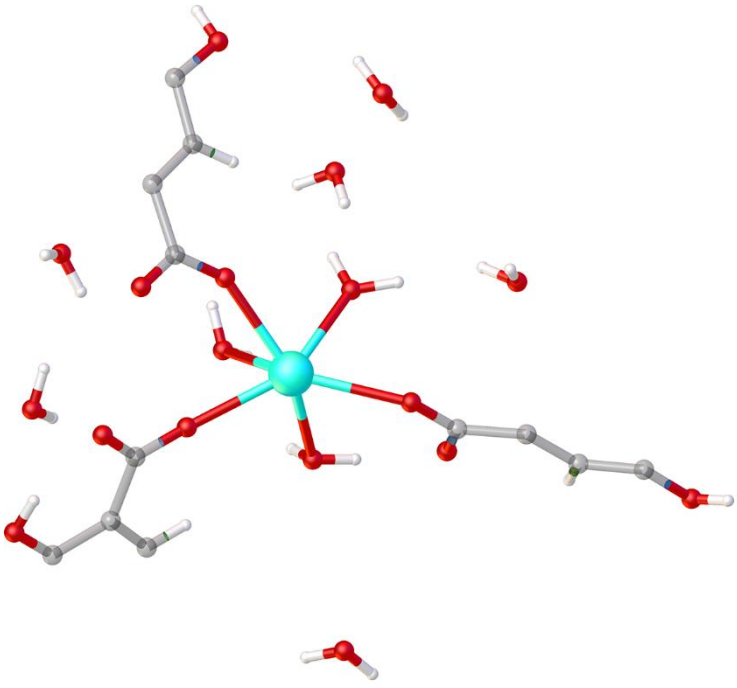

Figure S6 Asymmetry unit of **Gd-MOF**.

Table S1. Continuous shape measure analysis for eight-coordinated Ln^{3+} in **Tb-MOF** and **Gd-MOF**.

Eight-coordinated coordination sphere label	Shape	CSM parameters		Determined coordination geometry
		1	**2**	
OP-8	Octagon	29.520	29.436	
HPY-8	Heptagonal pyramid	24.202	24.221	
HBPY-8	Hexagonal bipyramid	16.559	11.339	
CU-8	Cube	16.566	11.749	
SAPR-8	Square antiprism	**1.272**	1.775	**SAPR-8**
TDD-8	Triangular dodecahedron	1.500	1.856	
JGBF-8	Johnson - Gyrobifastigium (J26)	14.365	28.985	
JETBPY-8	Johnson - Elongated triangular bipyramid (J14)	14.172	28.470	
JBTP-8	Johnson - Biaugmented trigonal prism (J50)	1.423	0.666	
BTPR-8	Biaugmented trigonal prism	1.362	**0.580**	**BTPR-8**
JSD-8	Snub disphenoid (J84)	3.926	12.100	
TT-8	Triakis tetrahedron	3.866	12.515	
ETBPY-8	Elongated trigonal bipyramid (see 8)	24.465	24.750	

Table S2. Selected bond lengths (Å) and angles [°] in **Tb-MOF**.

Parameters	**Tb-MOF**
Tb1-O1	2.3349(16)
Tb1-O4[1]	2.4046(16)
Tb1-O6	2.3603(16)
Tb1-O7	2.407(2)
Tb1-O8	2.3082(17)
Tb1-O9	2.3842(18)
Tb1-O10	2.4186(16)
Tb1-O12	2.3941(18)
Tb-O_{averge}	2.376
O1[1]-Tb1-O4[1]	72.52(6)
O1[1]-Tb1-O6	121.20(6)
O1[1]-Tb1-O7	73.06(7)
O1[1]-Tb1-O9	82.55(7)
O1[1]-Tb1-O10	137.47(6)
O6-Tb1-O7	140.49(8)
O6-Tb1-O9	140.46(7)
O7-Tb1-O10	126.19(6)
O9-Tb1-O12	93.42(8)

Symmetry code: [1]1-X,1-Y,1-Z; [2]-X,1-Y,1-Z; [3]1-X,-Y,1-Z; [4]2-X,-Y,-Z

Table S3. Selected bond lengths (Å) and angles [°] in **Gd-MOF**.

Parameters	**Gd-MOF**
Gd1-O1	2.329(3)
Gd1-O2	2.341(2)
Gd1-O3	2.431(2)
Gd1-O4	2.408(3)
Gd1-O5	2.445(3)
Gd1-O6	2.418(3)
Gd1-O8^{1}	2.409(3)
Gd1-O9^{1}	2.362(3)
Gd-O$_{averge}$	2.393
O1-Gd1-O2	81.39(10)
O1-Gd1-O3	138.39(10)
O1-Gd1-O4	144.50(11)
O2-Gd1-O3	136.38(10)
O2-Gd1-O6	143.13(11)
O3-Gd1-O5	126.59(10)
O4-Gd1-O6	91.00(13)
O6-Gd1-O3	71.48(10)
O6-Gd1-O5	70.21(12)

Symmetry code: ^{1}1-X,1-Y,1-Z; ^{2}-X,1-Y,1-Z; ^{3}2-X,-Y,-Z; ^{4}1-X,2-Y,1-Z

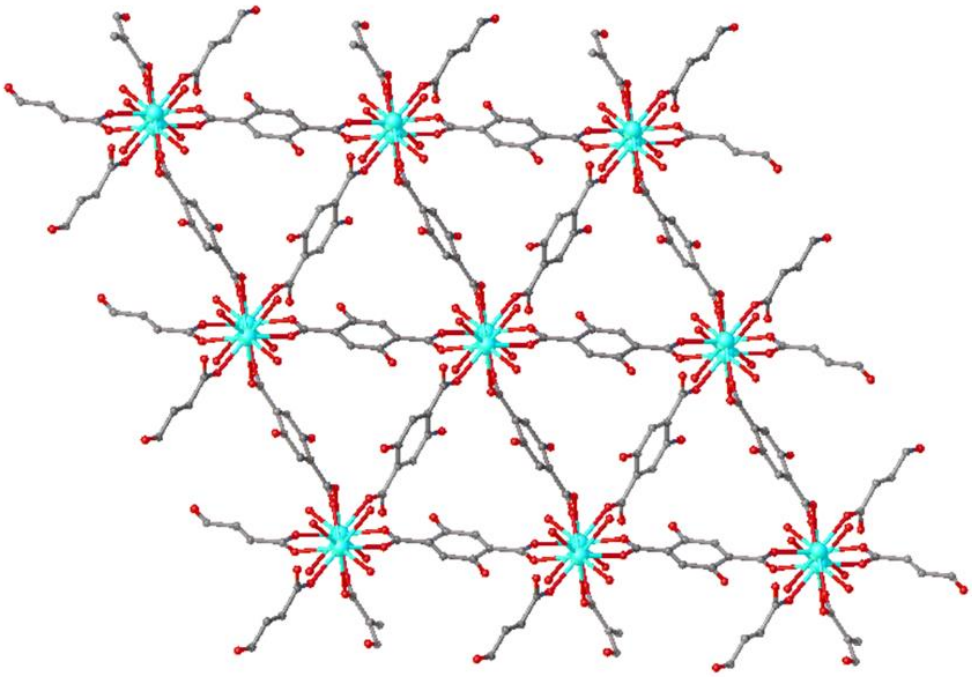

Figure S7. Portion of the 3D framework structure of **Gd-MOF**.

Topological analysis

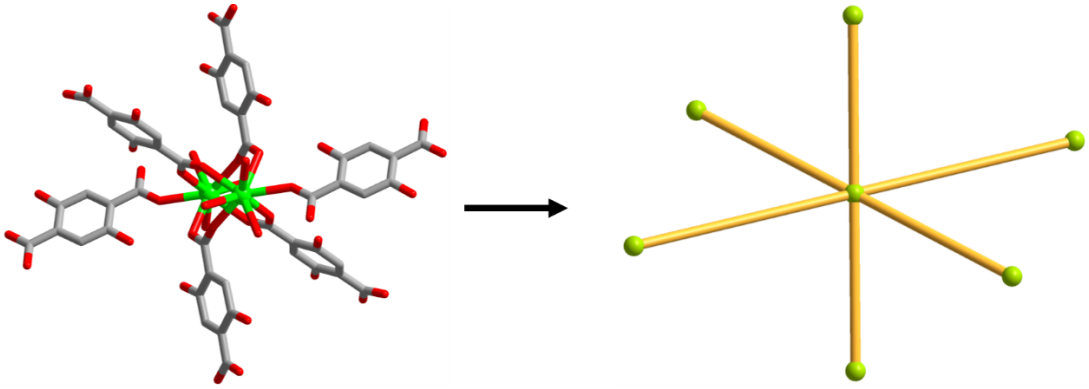

Prior to topological analysis, the structure has been simplified to its points of extension. The Tb_2 unit is reduced to a 6-connected (α) node. The Tb_2-MOF exhibits **pcu** topology.

Point symbol for net:$\{4^{12}.6^3\}$; 6-c net; uninodal net; transitivity: [1331]

Topological terms for each node:

(α) Point symbol: $\{4^{12}.6^3\}$

Extended point symbol:

[4.4.4.4.4.4.4.4.4.4.4.4.6(4).6(4).6(4)]

Coordination sequence: 6 18 38 66 102 146 198 258 326 402

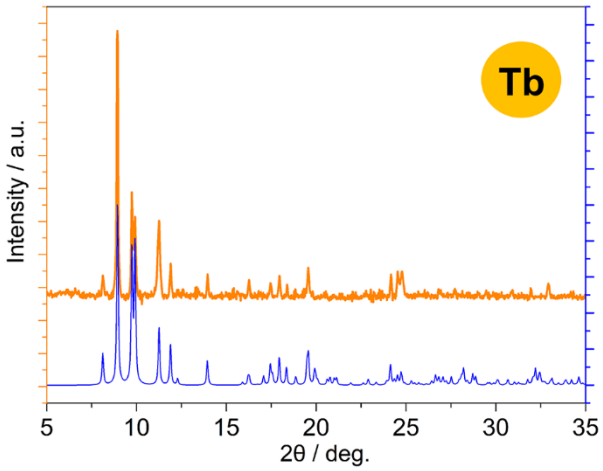

Figure S8. Comparison of the experimental PXRD pattern of **Tb-MOF** with the calculated pattern from the crystal structure.

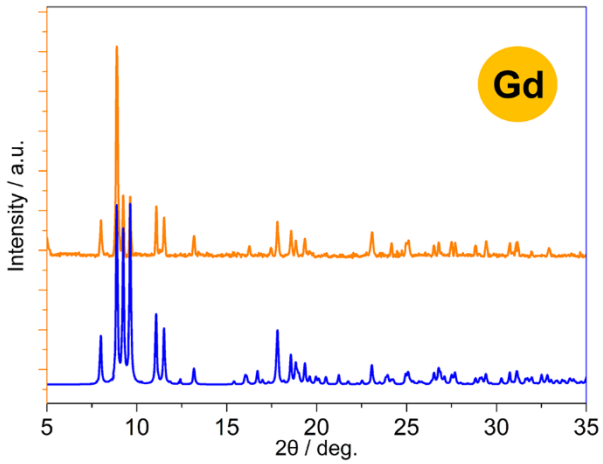

Figure S9. Comparison of the experimental PXRD pattern of **Gd-MOF** with the calculated pattern from the crystal structure.

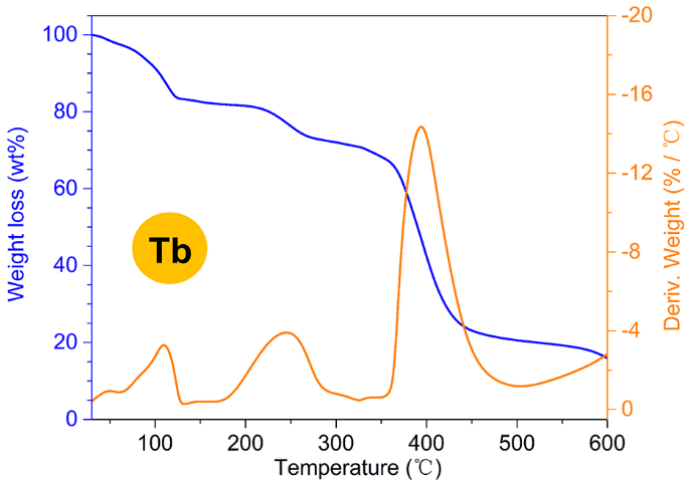

Figure S10. Termogravimetric analysis curve of **Tb-MOF**.

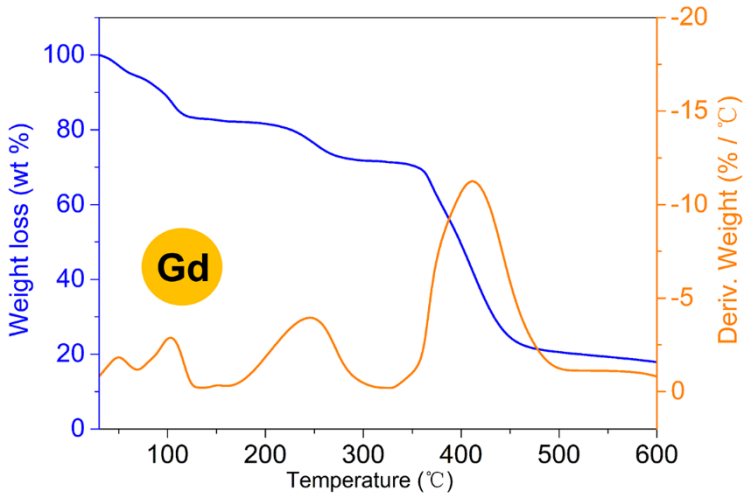

Figure S11. Thermogravimetric analysis curve of **Gd-MOF**.

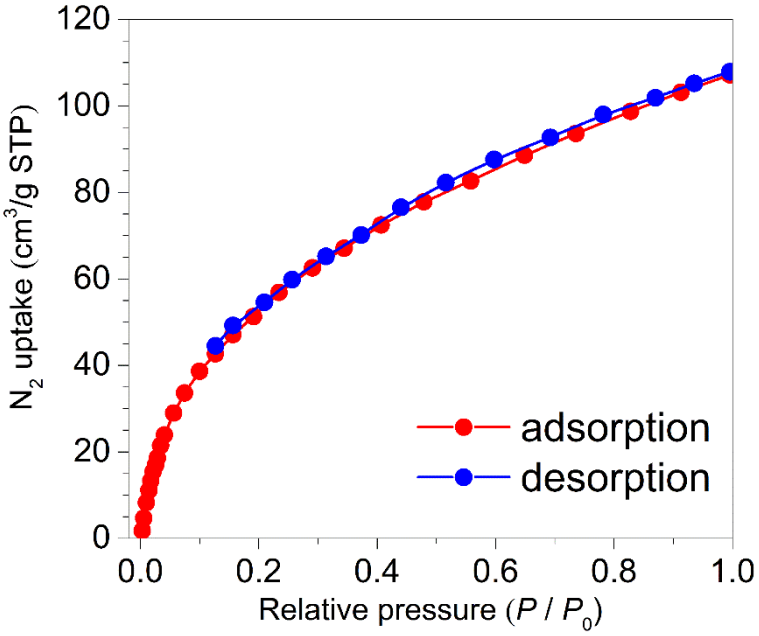

Figure S12. N_2 adsorption isotherms of **Gd-MOF** measured at 77 K.

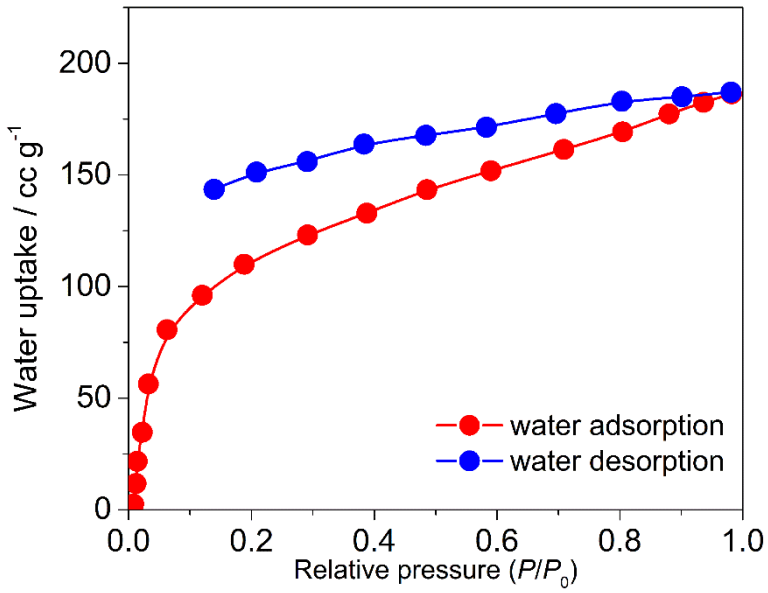

Figure S13. Water uptake of **Gd-MOF** measured at 300 K.

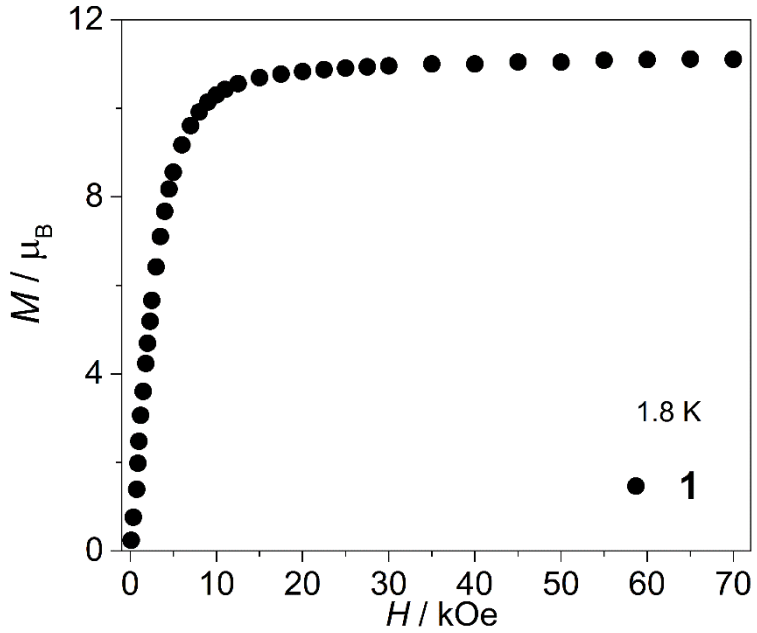

Figure S14. *M versus H* plot of **Tb-MOF** at 1.8 K.

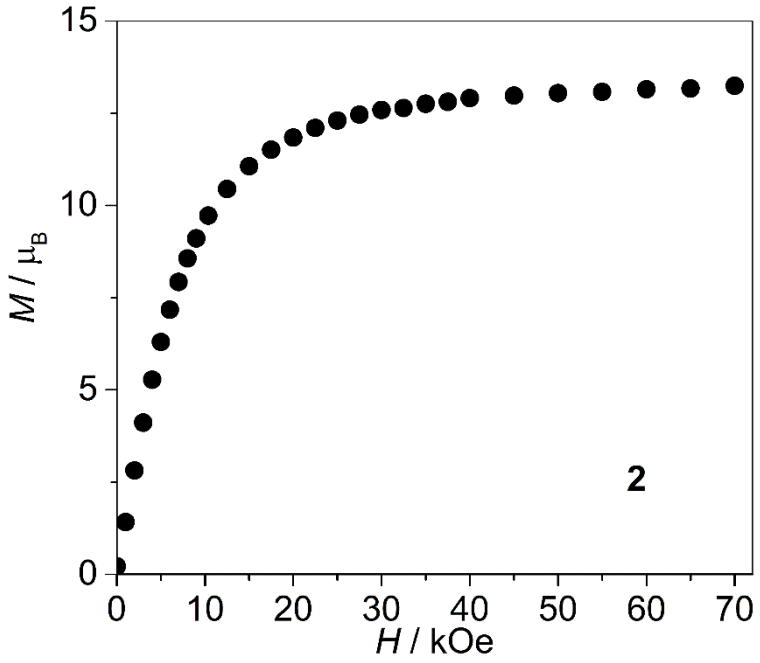

Figure S15. *M versus H* plot of **Gd-MOF** at 1.8 K.

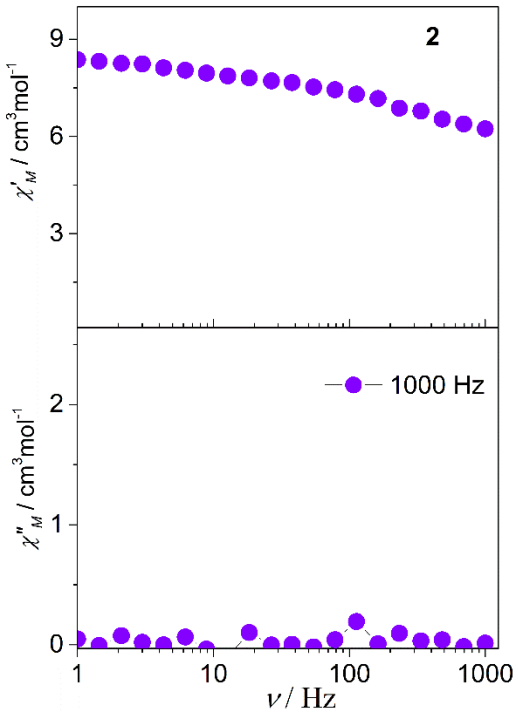

Figure S16. Frequency dependence of ac susceptibility measured under zero dc field at 2.0 K for **Gd-MOF**.

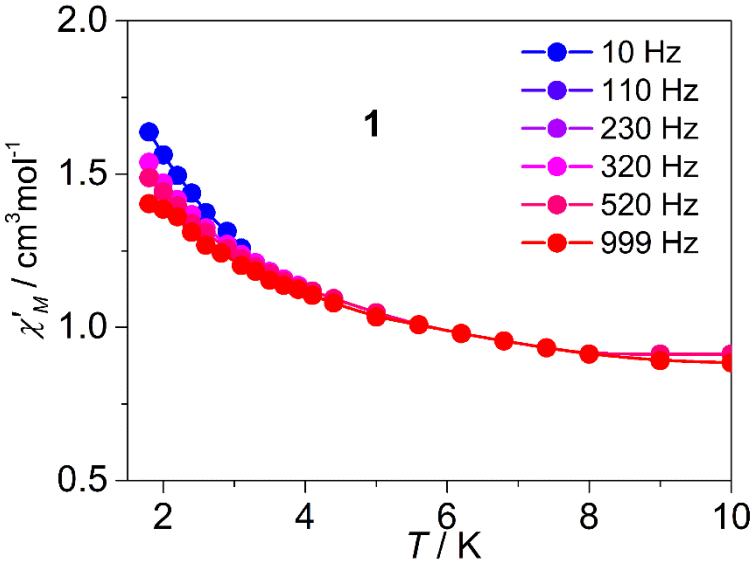

Figure S17. Frequency dependence of in-phase (χ′) signals ac susceptibility measured under zero dc field for **Tb-MOF**.

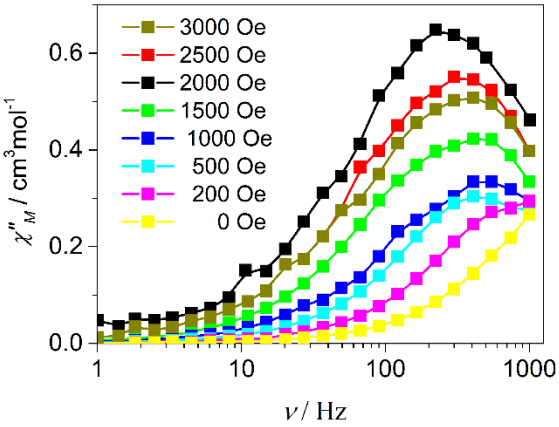

Figure S18. Frequency dependence of out-of-phase (χ″) signals ac susceptibility measured under different dc fields at 1.8 K for **Tb-MOF**.

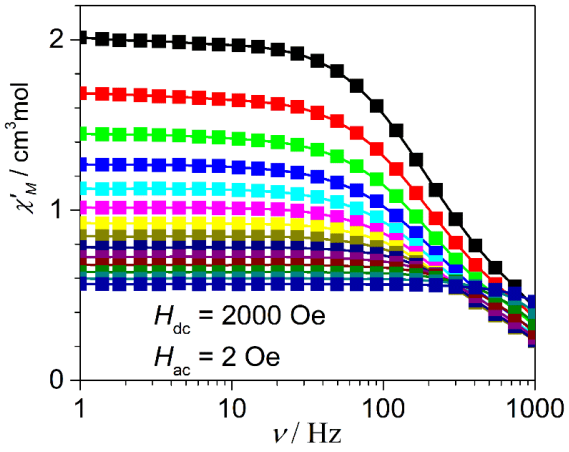

Figure S19. Frequency dependence of in-phase (χ′) signals ac susceptibility measured under 2 kOe dc field for **Tb-MOF**.

Table S4. Relaxation fitting parameters from the least-square fitting of the Cole-Cole plots of **Tb-MOF** under 2 kOe dc filed according to the generalized Debye model.

T / K	τ / s	χ_S / $cm^3mol^{-1}K$	χ_T / $cm^3mol^{-1}K$	α
1.8	0.0024	0.12343	0.57787	0.02966
2.0	0.00196	0.10694	0.56222	0.10408
2.2	0.00161	0.09218	0.53006	0.12493
2.4	0.00132	0.11059	0.47958	0.0496
2.6	0.00104	0.08602	0.43726	0.08904
2.8	8.52E-4	0.06822	0.40005	0.11004
3.0	7.08E-4	0.05142	0.39581	0.17072
3.2	5.64E-4	0.046	0.36356	0.04406
3.4	5.64E-4	0.0388	0.33206	0.04406

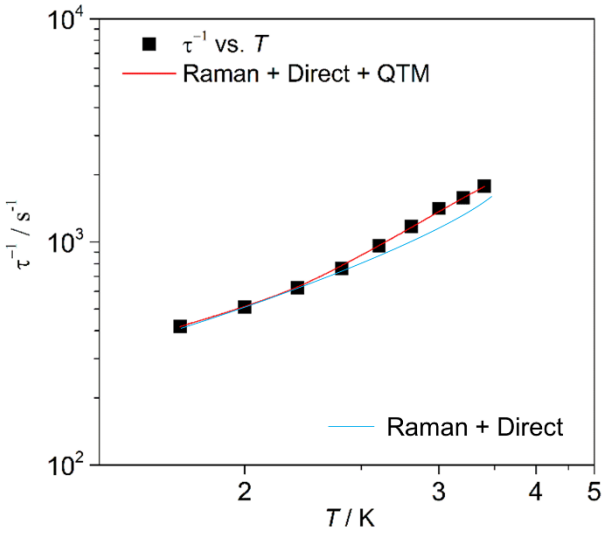

Figure S20. τ^{-1} vs T plot for **Tb-MOF**. The red line represents the fit via different relaxation mechanisms.

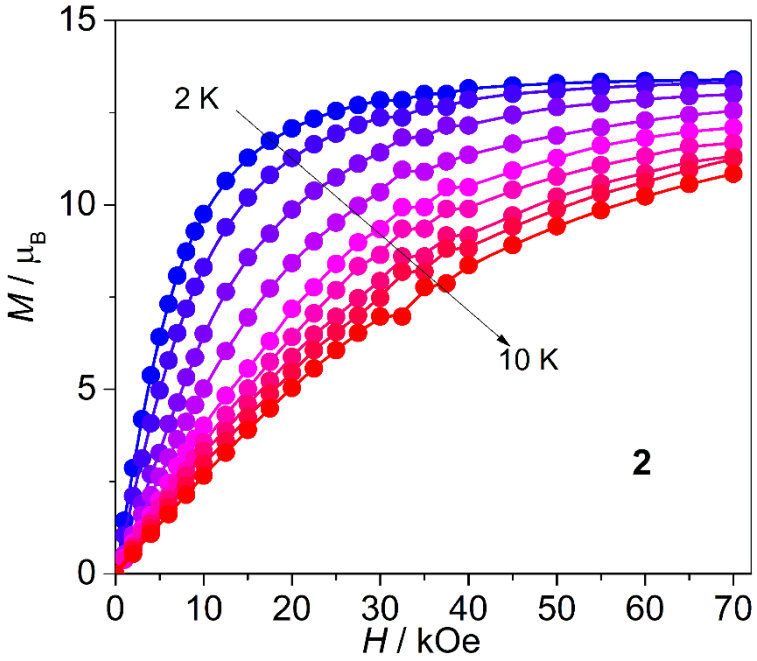

Figure S21. M versus H plots of **Gd-MOF** measured at 2-10 K.

Table S5. Some Reported Gd_2-based molecular coolants.

Compound	$-\Delta S_m$ J kg^{-1} K^{-1}	T_{max}	Structure	Ref
$[Gd_2(fum)_3(H_2O)_4]_n \cdot 3nH_2O$	20.7	5	3D	S5
$[Gd_2(N\text{-}BDC)_3(DMF)_4]_n$	29	7	3D	S6
$[Gd_2(OH)_2(suc)_2(H_2O)]_n$	42.8	7	3D	S7
$[\{Gd(OAc)_3(H_2O)_2\}_2] \cdot 4H_2O$	27	7	0D	S8
$\{Zn_2Ln_2(\mu_3\text{-}CO_3)_2L_2(acacF_6)_2\} \cdot CH_3OH$	12.6	7	0D	S9
$[Ln_2(\mu\text{-}Cl)_2(1\text{-}tza)_2(phen)_4](ClO_4)_2$	18.5	3	0D	S10
Ln_2Zn_6	11.25	2	0D	S11
$\{[Ln_2(H_2dhbdc)_3(H_2O)_8] \cdot 6H_2O\}_n$	20.2	2	0D	S12
$[Gd_2(O_2C^tBu)_6(HO_2C^tBu)_6]$	21.6	3	0D	S13

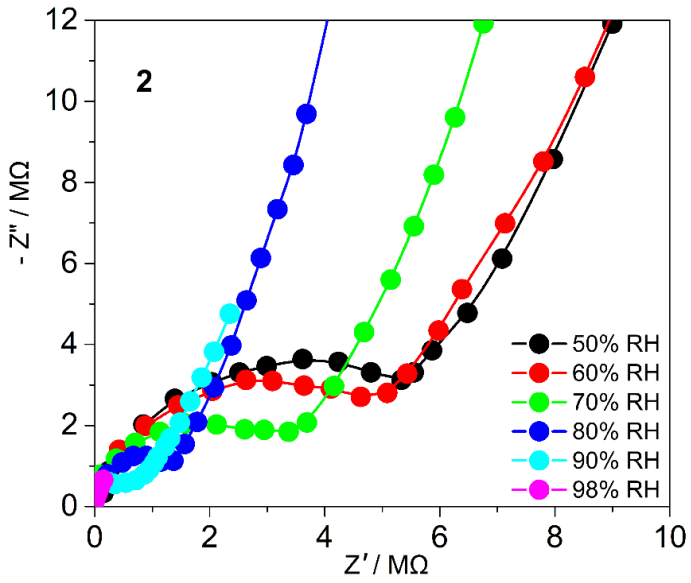

Figure S22. Nyquist plots of **Gd-MOF** at 30 °C under different RHs.

Table S6. Proton conductivity of **Tb-MOF** and **Gd-MOF** at 30 °C under various RH.

RH%	σ / S cm^{-1}	
	Tb-MOF	Gd-MOF
50	3.42×10^{-7}	1.43×10^{-6}
60	1.12×10^{-6}	2.72×10^{-5}
70	3.84×10^{-6}	8.61×10^{-5}
80	6.41×10^{-6}	1.86×10^{-4}
90	8.15×10^{-6}	2.72×10^{-4}
98	1.21×10^{-5}	4.21×10^{-4}

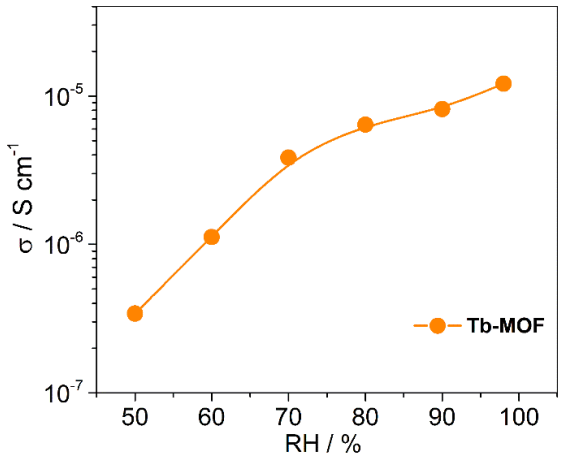

Figure S23. The humidity dependent σ at 30 °C of **Tb-MOF**.

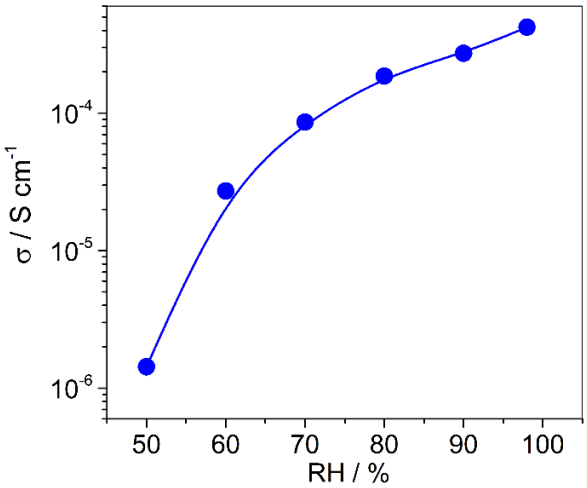

Figure S24. The humidity dependent σ at 30 °C of **Gd-MOF**.

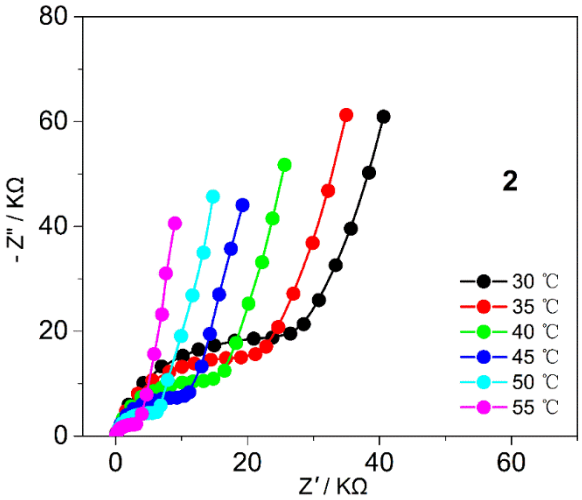

Figure S25. Nyquist plots of **Gd-MOF** measured under 98% RH at different temperature.

Table S6. Proton conductivity of **Tb-MOF** and **Gd-MOF** at varying temperature under 98% RH.

T / °C	σ / S cm^{-1}	
	Tb-MOF	Gd-MOF
30	1.23×10^{-5}	4.17×10^{-4}
35	3.95×10^{-5}	6.95×10^{-4}
40	5.22×10^{-5}	2.42×10^{-3}
45	6.63×10^{-5}	5.33×10^{-3}
50	4.17×10^{-4}	8.32×10^{-3}
55	1.63×10^{-2}	2.51×10^{-2}

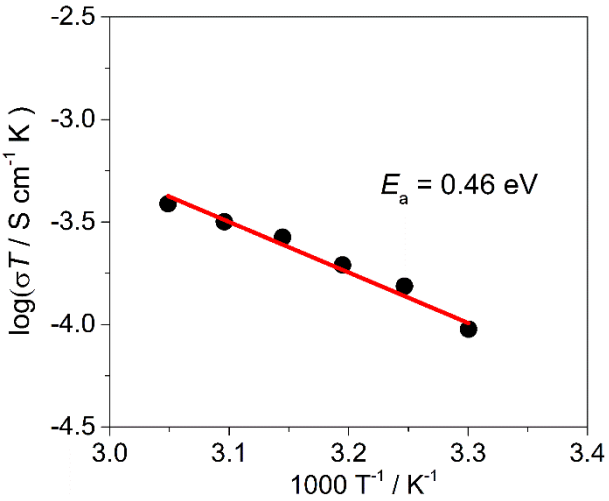

Figure S26. ln(σ*T*) vs. 1000/*T* for **Gd-MOF** at 98% RH.

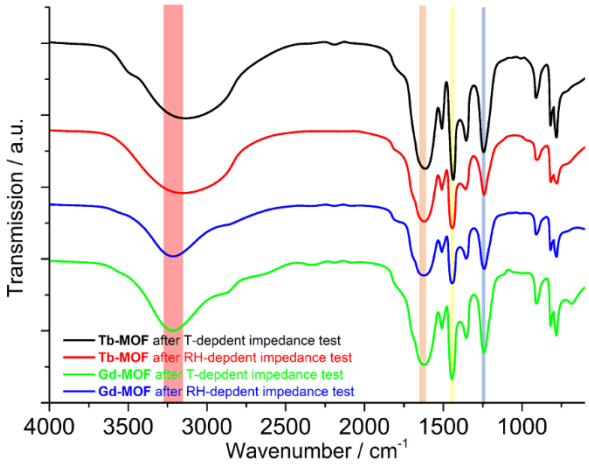

Figure S27. The FT-IR spectra of the **Tb-MOF** and **Gd-MOF** after electrochemical tests.

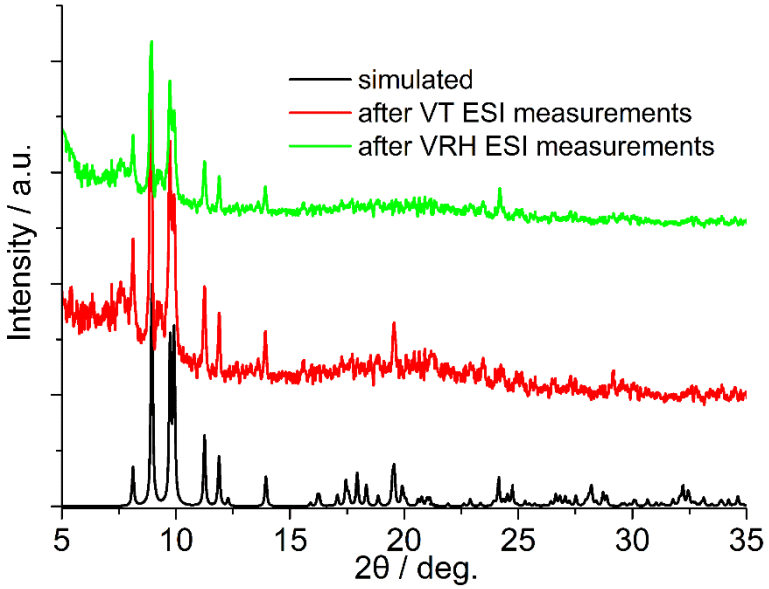

Figure S28. PXRD pattern of **Tb-MOF** after electrochemical tests.

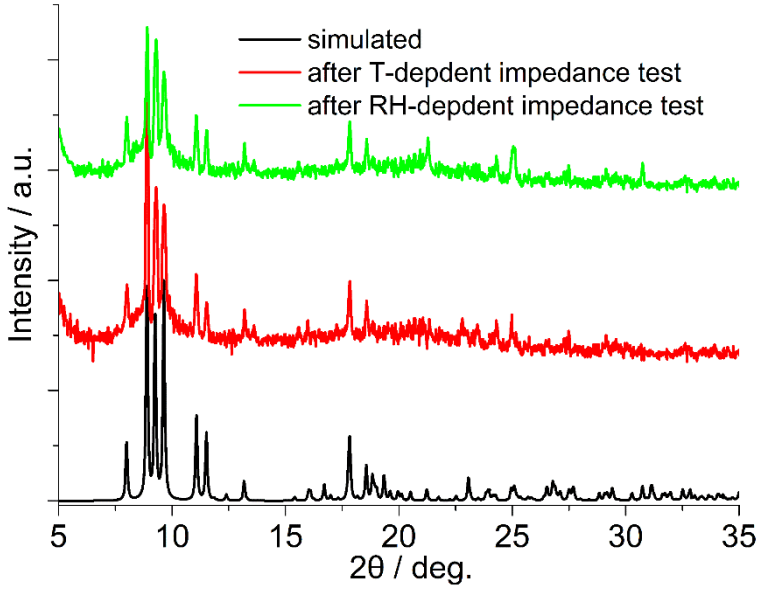

Figure S29. PXRD pattern of **Gd-MOF** after electrochemical tests.

References

S1) SAINT Software Users Guide, version 7.0; Bruker Analytical X-Ray Systems: Madison, WI, 1999.

S2) G. M. Sheldrick, SADABS, version 2.03; Bruker Analytical X-Ray Systems, Madison, WI, 2000.

S3) G. M. Sheldrick, SHELXTL, Version 6.14, Bruker AXS, Inc.; Madison, WI 2000-2003.

S4) Dolomanov, O. V.; Bourhis, L. J.; Gildea, R. J.; Howard, J. A. K.; Puschmann, H. OLEX2: A Complete Structure Solution, Refinement and Analysis Program. J. Appl. Crystallogr., **2009**, 42, 339−341.

S5) M. Evangelisti, O. Roubeau, E. Palacios, A. Ca, T. N. Hooper, E. K. Brechin, J. J. Alonso, Cryogenic Magnetocaloric Effect in a Ferromagnetic Molecular Dimer. *Angew. Chem. Int. Ed*. **2011**, 50, 6606 –6609.

S6) L. Sedlakova, J. Hanko, A. Orendacova, M. Orendac, C. L. Zhou, W. H. Zhu, B. W. Wang, Z. M. Wang, S. Gao, Magnetism and magnetocaloric effect in S = 7/2 Heisenberg antiferromagnet $Gd_2(fum)_3(H_2O)_4 \cdot 3H_2O$. *J. Alloys Compd*. **2009**, 487, 425-429.

S7) G. Lorusso, M. A. Palacios, G. S. Nichol, E. K. Brechin, O. Roubeau, M. Evangelisti, Increasing the dimensionality of cryogenic molecular coolers: Gd-based polymers and metal–organic frameworks. *Chem. Commun*. **2012**, 48, 7592–7594.

S8) Y.-C. Chen, F.-S. Guo, Y.-Z. Zheng, J.-L. Liu, J.-D. Leng, R. Tarasenko, M. Orendc, J. Prokleska, V. Sechovsky, M.-L. Tong, Anion-Templated Assembly and Magnetocaloric Properties of a Nanoscale $\{Gd_{38}\}$ Cage versus a $\{Gd_{48}\}$ Barrel. *Chem.–Eur. J*. **2013**, 19, 14876.

S9) C.-M. Liu, D.-Q. Zhang, X. Hao, D.-B. Zhu, Zn_2Ln_2 complexes with carbonate bridges formed by the fixation of carbon dioxide in the atmosphere: single-molecule magnet behaviour and magnetocaloric effect. *Dalton Trans*. **2020**, 49, 2121–2128.

S10) L. Dong, Y.-B. Lu, S.-D. Zhu, J.-W. Wu, X.-T. Zhang, Y. Liao, C.-M. Liu, S.-J. Liu, Y.-R. Xie, S.-Y. Zhang, A new family of dinuclear lanthanide complexes exhibiting luminescence, magnetic entropy changes and single molecule magnet behaviors. *CrystEngComm* **2021**, 23, 645-652

S11)S. Saha, K. S. Das, T. Sharma, S. Bala, A. Adhikary, G.-Z. Huang, M.-L. Tong, A. Ghosh, B. Das, G. Rajaraman, R. Mondal. Synergistic Experimental and Theoretical Studies of Luminescent-Magnetic Ln_2Zn_6 Clusters. *Inorg. Chem*. **2022**, 61, 2141−2153

S12)Q. Zhang, S.-Y. Yang, S.-J. Chen, L. Shi, J. Yang, Z. Tian, Z. Ruan, D. Shao, Lanthanide dimers in coordination chains constructed by sole dicarboxylate ligand for single-molecule magnet behavior and magnetocaloric effect. *J Mol. Struct*. **2023**, 1294, 136349.

S13)Y.-Q. Zhai, W.-P. Chen, M. Evangelisti, Z. Fu, Y.-Z. Zheng, Gd-based molecular coolants: Aggregating for better magnetocaloric effect. *Aggregate*. **2024**, e520.